Pressure-sensitive conversions between Cassie and Wenzel wetting states on a nanocorrugated surface

D. Vanzo[1], A. Luzar[1,2] and D. Bratko[1,*]

Abstract

Molecular dynamics simulations were used to study pressure-controlled wetting behavior of a nanostructured surface. Model graphene-like material functionalized by nanosized asperities was shown to support reversible dynamic transitions between superhydrophobic Cassie states that minimize contact with water and completely wetted Wenzel states. In practical applications, similar reversibility has been achieved by hierarchical corrugations, air trapping, or tailored geometry of surface posts. Nanocorrugations alone are shown to secure a robust Cassie state at low pressures, support transition to Wenzel state at pressure of $O(10^2)$ atm and can recover the Cassie regime without prohibitive hysteresis upon decompression. For O(10) nm surface fragments, timescales of dynamic response to compression deduced from the relaxation rates of water uptake fluctuations were estimated in the range of 0.1-1 ns. On small surfaces, an essentially barrier-free transition to Wenzel state is typically initiated at surface edges, followed by cooperative spreading across the entire surface. Conversely, the recovery of the Cassie state, which involves mild hysteresis, relies on nucleation away from the edges and should therefore be essentially independent of surface size. In conventional picture, cycling rate is determined by the latter process. This suggests subnanosecond responses of surface wettability could also be realized on macroscopic samples, leaving pressure control as the practical rate determinant in eventual application.

*dbratko@vcu.edu

[1]Department of Chemistry, Virginia Commonwealth University, Richmond, Virginia 23221, United States

[2]Deceased on March 5, 2019

1 Introduction

Tunable wettability is of interest in a host of applications [1, 2] ranging from micro- and nanofluidics [3, 4] to surface energy storage [5, 6]. Superhydrophobic materials offer two key advantages for the design of tunable surfaces, high sensitivity of wetting properties to external stimuli and potential for reversible control [1, 2, 7-10]. Superior sensitivity is associated with the ability of the surface to transition between two distinct wetting states: the fully wetted Wenzel state that maximizes the liquid/solid contact through complete wetting of surface corrugations, and the Cassie state, where liquid/solid contact is restricted to the tips of asperities while the remaining projected area of the surface constitutes of liquid/gas interface [11-13]. Conventional stimuli used to induce the Wenzel state include compression [8, 10, 14, 15] or applied voltage [16-19] (Fig. 1).

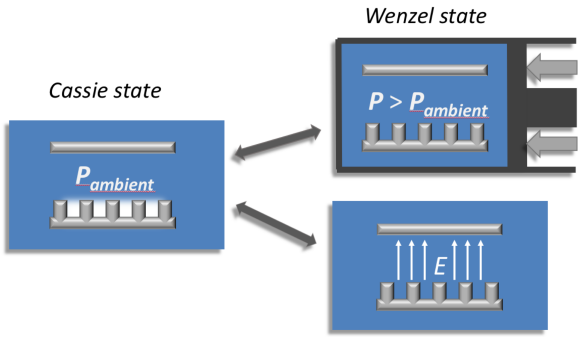

Fig. 1 Transition between Cassie and Wenzel wetting regimes under compression or electric field.

To secure the recovery of the Cassie state when the perturbation is removed, Cassie state should represent the global free energy minimum at ambient conditions, *and* the activation barrier between the two states should be surmountable by thermal fluctuations. At prevalent experimental conditions, the transition to Wenzel state is typically irreversible due to prohibitive kinetic barriers to the transition reversal[20]. Reducing the lengthscale of surface corrugations is instrumental in meeting the stated thermodynamic *and* kinetic requirements [10, 13, 21, 22]. In an earlier work we showed the descent to subnanometer dimensions of surface features (wells and pillars) to be particularly effective [21], securing a stable Cassie state even when the surface material is moderately hydrophilic in the absence of corrugations. At the same time, small surface-well dimensions result in lower activation barriers to water expulsion from the wells. Unlike the thermodynamic condition for the stability of either wetting state, which generally depends on

relative (intensive) properties like surface coverage by asperities (*f*), Wenzel roughness (*r*), and the aspect ratio of the pillars, the kinetic barrier to the well-by-well evacuation[23, 24] on a fully submerged substrate (to be compared to thermal energy k*T*) decreases in parallel with the *absolute* size of the corrugations. The descent to the nanoscale thus combines high sensitivity *and* rapid response of wetting properties to changing conditions [21]. In view of experimental challenges at extreme miniaturization, our previous works relied on molecular modeling as a valuable complement to direct experiments in this regime. Using Molecular Dynamics simulations, we have identified a range of nanocorrugation topolographies conducive to stable Cassie states [21] and their modulation by electrowetting [19]. In the present study, we explore wetting responses to pressure as a driving force for the Cassie-to-Wenzel transition. We use an adaptation of the simulation setup from ref. [19], with the superhydrophobic surface representing one of the walls of a fixed-size confinement inside a pressurized bath. Our computer experiments manifest the ability of sub-nano corrugations to satisfy two conflicting requirements: keeping surface wells sufficiently wide to wet at experimentally feasible pressures, yet small enough to avoid prohibitive hysteresis during the recovery of the Cassie state upon decompression.

Temporal responses to pressure changes were characterized in terms of correlation times associated with the fluctuations of the order parameter quantifying the extent of wetting of the corrugated surface. Comparison between observed transition rates at different surface dimensions indicate a moderate slowdown with increasing surface size. The observed size dependence is consistent with cooperative expansion or shrinking of contiguous regions dominated by either of the two states. The Wenzel state is typically initiated at surface edges in contact with bulk water, followed by propagation to the surface center, whereas the transition to Cassie state relies on homogeneous nucleation. This difference is expected to disappear on bigger surfaces where both transitions should depend on homogeneous nucleation events leading to asymptotic response rates in macroscopic limit. In analogy with electrowetting transitions [19], the insights from our dynamic simulations support the notion of local Wenzel-to-Cassie transitions as the slower of the two nucleation processes because of the kinetic barrier to water expulsion from surface wells. Implications of present results for the behavior of macroscopic systems are discussed in the light of this observation.

2 Model and Methods

2.1 Simulation setup

To secure a robust Cassie state at low pressures, we employed the topography and intermolecular potentials introduced in an earlier study at ambient conditions [21]. The nano-corrugated surface was represented by a graphene-like carbon sheet decorated by four-atom asperities carved out of (hypothetical) 2nd and 3rd layers of graphite. The height of the asperities (~8.3 Å) hence corresponds to twice the interplane distance of 3.4 Å in graphite, enlarged by the Lennard-Jones radius of carbon. The pillars contain a pair of covalently bonded carbon atoms at each of the two heights of protrusion, giving the asperities the (projected) size of about 4.4 Å x 4.6 Å. The projected dimensions exceed the diameter of carbon atoms because of the added width corresponding to the length of the covalent bond between a pair of atoms at each height *and* the slight tilt of the posts associated with the shift of consecutive carbon layers in graphite. Consistent with the underlying carbon lattice, the asperities are planted periodically at separation 8.5 Å along *x* and 9.8 Å along *y* direction (Fig. 2). The stoichiometric fraction of graphene atoms supporting the asperities is 1/16,

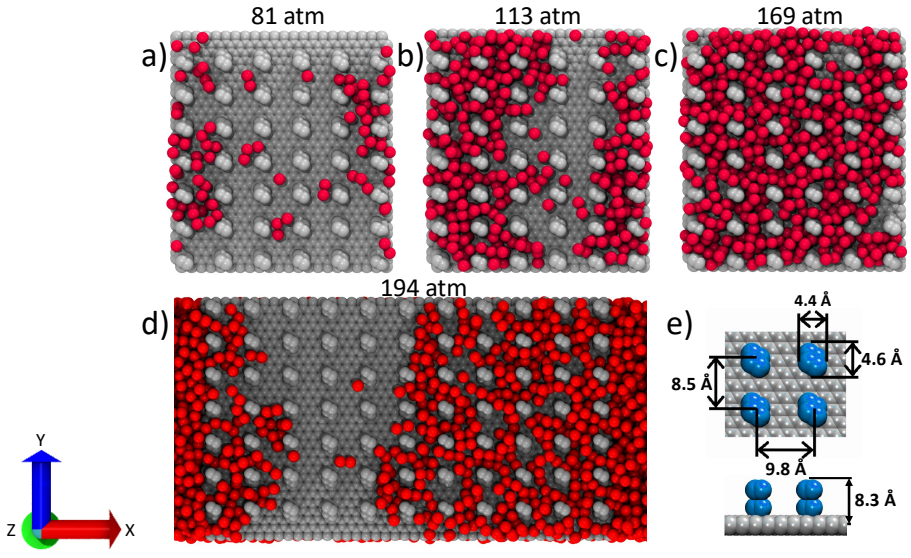

Fig. 2 Snapshots of the smaller corrugated surface in Cassie (a) and Wenzel (c) states, and of systems of both sizes during the Cassie-to-Wenzel transition (b and d). Grey: carbon atoms, red: oxygen atoms of water between the asperities. For easier visualization, the snapshots omit all hydrogen atoms and oxygen atoms above the height of the asperities. Surface widths along *x* direction are 54 Å (a-c) or 102 Å (d), respectively. The infinite surface size along *y* axis arises through periodic replication of the box in *y* direction. (e) Details of the corrugations: the size of graphene atoms (gray) is determined by the length of the covalent CC bond and that of the asperity atoms (blue color in panel e) by the Lennard-Jones diameter of carbon atoms.

leading to the projected surface fraction of the asperities *f* close to 1/7. The difference between the two fractions is explained by larger Lennard-Jones (LJ) size of carbon atoms (~ 3.24 Å) [25] compared to 1.42 Å spacing among covalently bonded atoms inside graphene [26]. The projected area of a dumbbell comprised of a pair of carbon atoms with center-to-center distance of 1.42 Å and Lennard-Jones atom diameter 3.24 Å is ~12.3 Å^2 whereas the area per carbon atom in graphene is only 2.62 Å^2 (5.24 Å^2 area for a pair of atoms). The Wenzel roughness factor *r*, defined as the ratio of the solvent-accessible areas[27] of the corrugated and pillar-free substrates, is estimated at ~ 4. Following refs.[27-30], the solvent accessible area is measured at the surface enveloping the region sterically excluded to the centers of water molecules, which extends ~1.6 Å (the radius of water molecule) beyond the pillar dimensions shown in Fig. 2. In the continuum picture and for ambient conditions, the above fractions f and r render the Cassie state stable for materials with $-\cos\theta > \frac{1-f}{r-f} = 0.22$, or $\theta > 102.7^{o}$ [11] and monostable [31] if the same inequality is also satisfied by the receding contact angle θ_r for given material (θ denotes contact angle on flat surface). Our material's θ is ~110^{o} and shows negligible contact angle hysteresis[21]. As shown in the next section, all-atom simulations for our model surface at room conditions affirm the prediction of stable Cassie state derived[11] from macroscopic arguments. The specified surface structure is described in Fig. 1 (system 3) of earlier work [21], which provides a systematic comparison between distinct corrugation topographies. Fig. 2 in the present article shows corrugation dimensions and snapshots of the surface at varied degrees of wetting for two system sizes we considered. The surface had finite width D_x of 54 Å in the smaller and 102 Å in the bigger system. These values correspond to 6 and 11 lines of posts, or 5 and 10 grooves along the *y* direction, respectively. A groove is defined as sequences of "wells", and well as the free space between four adjacent pillars. Because of finite spacing between the pillars, the wells are partially open to each other. Their wetting states are therefore affected by that of their neighbors. The length of the surface along y axis is presumed infinite (modeled by periodic replication of 59.6 Å long fragments in *y* direction). The simulation box size L_y was hence 59.6 Å. The width of the box in *x* direction, L_x, was approximately twice bigger than the surface width in *x* direction, D_x, ($L_x = 102$ Å in the smaller and 200 Å in the bigger system). The height of the box ($Z \equiv L_z$) was varied within the interval of ~ 75–105 Å to control the pressure in the box. The number of water molecules was 13,494 in the smaller and 31,075 in the bigger system.

2.2 Methods and force fields.

Molecular dynamics (MD) simulations were carried out using LAMMPS software [32] with 11 Å cutoffs of real space electrostatics and LJ interactions. Long-range coulombic forces were determined using the PPPM algorithm with slab correction to account for the two-dimensional periodicity of our system [33]. The timestep of the simulation was 2 fs. Nose-Hoover thermostat [34] was used to keep temperature at 300 K whereas we used NVE sampling in time correlation calculations.

Direct imposition of desired pressure by standard barostats like Nose-Hoover barostat [34] proved implausible in the strongly fluctuating regime near the superhydrophobic threshold. Compression was therefore enforced by adjusting the vertical distance Z between a pair of repulsive walls (w) placed at the bottom ($z_w = -Z/2$) and top ($z_w = Z/2$) boundaries of the simulation box to mimic the action of the piston indicated in Fig. 1. Repulsion between these walls and oxygen atom at the wall-oxygen distance $z_{wO}=|z_w-z_O| < z_c$ was described by the harmonic repulsion potential $U_{wO} = \varepsilon_h(z_{wO}-z_c)^2$ where the spring constant $\varepsilon_h = 4\cdot10^4$ J mol^{-1} Å^{-2} and the cutoff distance $z_c = 5$ Å. At distances $z_{wO} > z_c$, $U_{wO}=0$. Because of the walls' hydrophobicity, the fluid layer next to box walls shows density depletion [35] and increased compressibility [36-39]. As discussed in the following section, this contributes to the reduction in the height Z required for specific increase of pressure and penetration of water into the surface wells.

To keep the geometry of water slab above the superhydrophobic surface unchanged irrespective of changes of box height Z, a hydrophilic wall of equal dimensions and graphene-like structure was placed at the height z 40 Å from the corrugated surface, so the two surfaces were located at heights $z = \pm 20$ Å with the box midplane at z=0. This way, pressure throughout the entire box was controlled by volume changes of the regions below the corrugated surface and above the upper wall without modifying the water slab in direct contact with the corrugated surface. While the model setup accommodated changes of distance Z between the lower and upper wall, the structure of all walls was fixed during entire simulation.

Following previous works [19, 21, 40-44], we modeled water using the SPC/E potential[45] and carbon atoms were parameterized according to Werder et al. [25] (systems 1-7 of that work), with

LJ energy and size parameters for carbon-oxygen interaction ε_{CO}=0.314 kJ mol^{-1} and σ_{CO}=3.19 Å. The above parameters produce contact angle θ on a perfectly smooth surface ~ 110±3° and ~150±10° on corrugated surface in the Cassie state. These values were determined [19, 21] from the average nanodroplet contours as described elsewhere[40, 46-48]. For the opposite (hydrophilic) surface at the height z=20 Å we used the energy parameter ε'_{CO}=0.56 kJ mol^{-1}, which corresponds [48] to contact angle close to 50°.

3 Results and Discussion

3.1 Stability against capillary evaporation. In view of strong hydrophobicity (Cassie state contact angle θ_1 ~ 150°) of the corrugated surface at z = -20 Å, we first verify the stability of liquid state for water in the pore between this surface and the opposite hydrophilic (θ_2 ~ 50°) wall at z = 20 Å. Continuum estimate for the capillary-evaporation threshold width d_c in an asymmetric pore was shown[49] to follow the relation $d_c \sim -2(A/C)\langle\cos\theta\rangle$. Here, A is the nanopore wall area (in our case D_xD_y), C is the wall circumference (due to periodic replication along y axis in our system, $C = 2D_y$ and $2A/C=D_x$), and $\langle\cos\theta\rangle = (\cos\theta_1 + \cos\theta_2)/2$. The omission of edge length along x direction follows from applied periodic conditions. Through replication along y axis, the surface acquires the shape of infinite stripe without exposed edges along x direction. An equivalent prediction for walls of square geometry is given in ref.[50]. For present contact angles and wall sizes, we obtain d_c ~ 6 Å for the smaller and ~11.5 Å for the bigger system. For both system sizes, the separation between the height of the asperity tips (z ~ -12 Å) *and* the upper confinement wall at the height z=20 Å is well above d_c even in the Cassie regime. The stability of liquid phase is confirmed in explicit simulation at ambient pressure. When started from initially evacuated-pore configurations, the pore was consistently filled by spontaneous infiltration of water from the surrounding bath. In these runs, the intrusion of water typically begun at the upper, hydrophilic wall. Once this wall was fully wetted, the infiltration continued by wetting the (lower) corrugated surface from the edges toward the center until achieving a complete Cassie state. Fig. 3 illustrates an intermediate stage of this process. Fig. 3 shows an intermediate stage of this process. Spontaneous intrusion of water is observed at even smaller pore widths than considered in systems shown in Figs. 2 and 3. The process is visualized in a video file "infiltration.mpg" included in the Supplementary Information (SI).

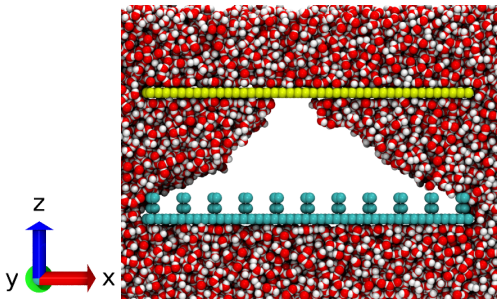

Fig. 3 Snapshot of a partially filled state during spontaneous intrusion process of water into an initially empty pore in contact with a reservoir at ambient conditions.

3.2 Cassie-Wenzel transition. The final configuration obtained in the trial runs described above, corresponded to Cassie state we used as the starting point in a series of runs with changing pressure. In these runs, pressure in the confinement was gradually increased from the ambient value to ~ 300 atm by decreasing the separation between the two repulsive walls at horizontal box boundaries. At the beginning of each run, molecular velocities were randomized and the system re-equilibrated at ambient pressure. To confirm the transition between the Cassie and Wenzel states can be reversed, we monitored compression (decreasing *Z*) and decompression (increasing Z) processes. We considered two rates of change in *Z*, $dZ/dt = \pm 7$ Å ns^{-1} or ± 3.5 Å ns^{-1}. In view of slow sampling of simulated pressures, constantly changing pressure values could not be reliably determined during the cycles at given rates. Separation *Z* was therefore used as the measure of compression. To relate *Z* to the pressure, in separate equilibrium simulations, we calculated average pressures for a set of constant heights *Z* in the vicinity of the wetting transition. Considering the tensorial character of pressure in our interfacial system, we chose to monitor the vertical component of pressure, $<P_z>$, which directly controls the intrusion of water [51, 52] into the wells between vertical asperities on the corrugated surface. At each of a set of equidistant heights *Z*, virial pressure was sampled over 14 ns in the smaller and 22 ns in the bigger system with data collected in 50 ps intervals. This interval size proved sufficient to avoid correlations among successive pressure values. A statistical analysis leads to estimated standard deviation *of the mean* pressure between 4 -7 atm.

We follow the transition between two wetting states by monitoring the relative filling index defined [19] as the ratio $N(Z)/N_w$ between the average number of water molecules inside the surface grooves at specified Z, $N(Z)$, and the corresponding number at the beginning of the plateau branch

of $N(Z)$ in the Wenzel regime. With this definition, N_w is 275 for the smaller and 600 for the bigger surface, respectively. This corresponds to approximately ten water molecules per well at the lowest pressure inducing the Wenzel state. In addition to the uptake of water by the wells, the changes of the net volume (L_xL_yZ) comprise two additional contributions. Because the top and bottom box walls are strongly hydrophobic, the fluid in a thin film next to these walls has reduced density and greatly increased compressibility [35-39, 51]. Total volume reduction at increased pressures reflects the contraction of the interfacial films at box boundaries, absorption of water inside the wells on the superhydrophobic surface, and slight contraction of bulk-like water away from the interfaces. For present system sizes, at the maximal pressure $P \sim 300$ atm, the three distinct effects are estimated to contribute around 65±5%, 20±3%, and 13±2% of net contraction, respectively.

Fig. 4 illustrates the wetting transition on the smaller surface (D_x=54 Å) at compression rate dZ/dt = ± 7 Å ns^{-1}. The six colors correspond to independent cycles, each started from a newly

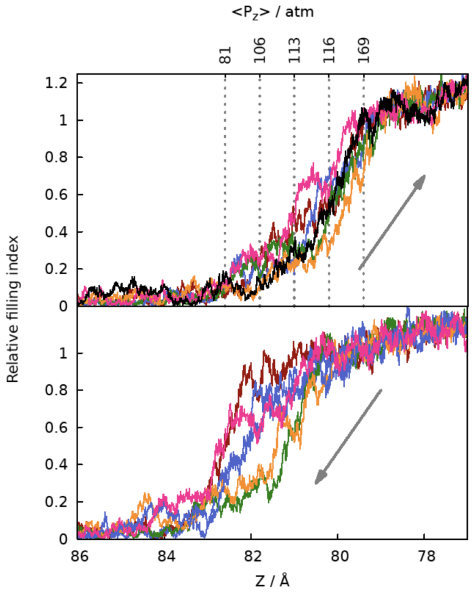

Fig. 4 Filling index measuring the degree of conversion from Cassie (index 0) to Wenzel state (index 1) as function of compression of confined water above the superhydrophobic surface in six independent cycles using the smaller of the two system sizes with D_x= 54 Å. Decreasing the separation between the top and bottom walls of the simulation box, Z, leads to compression (top), with transition to Wenzel state taking place within the pressure interval 80-160 atm. The rate of change in Z was ±7 Å ns^{-1}. The reverse process (bottom) leads to the recovery of Cassie state. The observed hysteresis reflects the activation barrier to expulsion of water from surface wells upon decompression. The finite slope observed in Wenzel regime reflects increased compressibility of interfacial water. Pressure averages at five relevant separations were determined in separate 14 ns runs for each of preselected Z values.

randomized initial configuration and molecular velocities. Dashed vertical lines denote equidistant heights Z at which we determined corresponding pressures <*Pz*> in equilibrium simulations. In order to examine how well can equilibrium pressures <*P*(*Z*)> represent conditions during the finite-rate compression process, we repeated the simulations illustrated in Fig. 4 at twice lower rate d*Z*/d*t* = = ± 3.5 Å ns^{-1}. Comparison between the results for the two different rates (Figs. 4 and 5) reveals only insignificant differences suggesting the pressure response to volume reduction is sufficiently fast to produce essentially converged results at the rates applied in our calculations. As such, average pressures <*P*(*Z*)> are deemed representative of actual pressures in the forward process corresponding to the Cassie-to-Wenzel (C2W) transition. In the smaller system, the transition begins at pressures P_z > 80 atm and completes around P_z ~ 160 atm. Snapshots of the corrugated layer of the surfaces taken during the C2W branch at pressures 81 atm, 113 atm, and 169 atm in the smaller, and 194 atm in the bigger system are shown in Fig. 2 a-d.

The reverse (W2C) branch describing water expulsion from the grooves upon decompression reveals hysteresis reflected in different intrusion and expulsion pressures (inflection points of *N*(*Z*)). The hysteresis is explained by the presence of a moderate activation barrier to water The reverse (W2C) branch describing water expulsion from the grooves upon decompression reveals

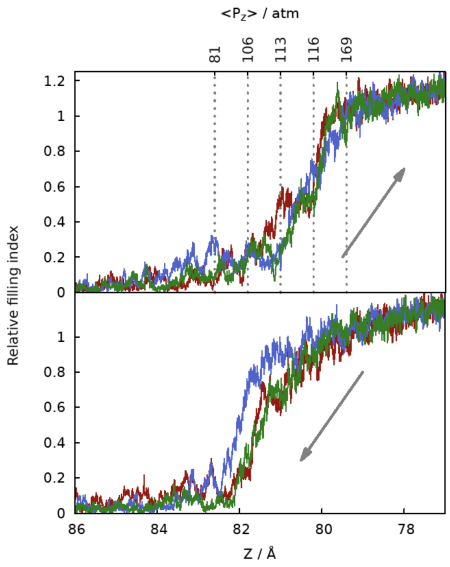

Fig. 5 Filling index in the compression (top)/decompression (bottom) branches for three independent cycles at the slower rate of change in *Z* of ±3.5 Å ns^{-1}. The similarity to the results for the higher rate of 7 Å ns^{-1}, shown in Fig. 4, indicates acceptable convergence with respect to the speed of the process.

hysteresis reflected in different intrusion and expulsion pressures (inflection points of $N(Z)$). The hysteresis is explained by the presence of a moderate activation barrier to water expulsion from the wells, $\Delta\Omega^* \sim \gamma a_{lv}$, associated with new liquid/vapor interface a_{lv} (surface tension γ) emerging in the evacuation process. A related effect has been discussed in context of capillary evaporation [23, 24, 35, 53, 54]. When the liquid evacuates from a well on a pillared surface, a_{lv} comprises the interface formed as the liquid detaches from the bottom of the well. In addition, a_{lv} should include any increase (or reduction) of liquid/vapor interface that may take place at the vertical openings between the pillars shared by adjacent wells. All neighboring wells are expected to contribute according to their types in approximately additive manner. The first term is absent during infiltration (C2W process), but results in a kinetic barrier when the process involves water expulsion (W2C process). As a result, the W2C transition behaves as an activated process. The second term, originating at the boundaries between adjacent wells, facilitates the change of wetting state if the well is predominantly surrounded by neighbors existing in the opposite (wetting) state and vice versa. Both forward (C2W) and backward (W2C) transitions therefore proceed in a highly cooperative manner. Irrespective of the direction, the second (well/well interface) term is essentially canceled out when the transition proceeds through propagation of the borderline (perimeter) between pure domains of either wetting state, merely shifting the position of the interface between the groups of wells existing in opposite wetting states. It can, however, impede the transition in the initial (nucleation) stage and accelerate its completion in the final stage.

As already indicated by the snapshots in Fig. 2, for otherwise identical conditions, wells on surface edges bordering bulk water phase are biased in favor of the water-filled (Wenzel) state. It was therefore of interest to assess the effect of size of the superhydrophobic surface on threshold pressures inducing the wetting-transition in either direction. In Fig. 6 we present results analogous to those shown in Fig. 4 but for the bigger system (D_x=102 Å). At both surface sizes, significant compression is required to impose (or preserve) the Wenzel regime, but more so on the bigger surface where both, the intrusion (C2W) and expulsion (W2C) pressures are considerably increased compared to the smaller one. This difference reflects weakened edge effects (favoring Wenzel state) on the bigger surface. 40% of surface wells are located on the edges on the smaller surface, while this group represents only 20% of all the wells on the bigger one. The behavior of the bigger system is hence much closer to the extended surface limit where border effects become

insignificant. The slightly nonmonotonic variation of $<P_z>$ with Z shown in Fig. 6 reflects statistical errors in pressure sampling (standard deviation of the mean 4 atm at D_x=102 Å). Conversely, the filling index *is* a monotonic function of the wall-to-wall separation Z, an input determinant of compression free of statistical uncertainties.

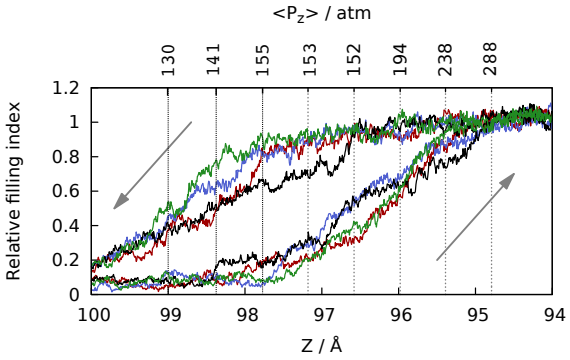

Fig. 6 Compression/decompression cycle determined in four independent runs for the bigger system (D_x=102 Å) at the rate of change in Z of $\pm$7 Å ns^{-1}. Pressures at a set of equidistant wall-wall separations Z were determined in 22 ns simulations runs for each of the fixed Z values. The compression required to support the Wenzel regime is higher than in the smaller system (shown in Figs. 4 and 5) where Wenzel state is additionally stabilized because a higher fraction of surface wells reside at the surface edges.

During compression, edge grooves are typically wetted first and the process proceeds cooperatively from the edges toward the surface center as already wetted wells facilitate the infiltration of water into nearby wells. While the C2W transition on a fully submerged surface lacks complete analogy with the CW transition under a drop with changing base area, it is of interest to compare our observations with reported C2W scenarios for the droplet geometry[55, 56]. Ishino *et al*. consider a transition with initial nucleation of the Wenzel state under the center of the drop and subsequent expansion toward the drop perimeter[56]. Conversely, Bormashenko et al. show the transition to be initiated at the perimeter followed by propagation toward the drop's base interior[55]. The C2W transition observed in our model calculations clearly follows the latter scenario, with the opposite sequence observed in the reverse (W2C) transition. A visualization of both processes is provided in the video CWcycle.mp4 in the Supplementary Information. To quantify the correlation between wetting states of neighboring wells as a function of distance, we monitored the spatial correlation function

$$C(r;P) = \frac{<\delta N_a(r_a;P)\delta N_b(r_b;P)>}{(<\delta N_a(r_a;P)^2><\delta N_b(r_b;P)^2>)^{\frac{1}{2}}} \quad (1)$$

where $N_a(r_a;P)$ is the number of water molecules residing inside the surface well at r_a at given pressure, $\delta N_a(r_a;P) = N_a(r_a;P) - <N_a(r_a;P)>$, and $r=|r_a-r_b|$. In Fig. 7, we present results for $C(r)$ determined in 14 ns runs by averaging over all combinations of well pairs in the smaller system size at five pressures specified in Fig. 4. Consistent with the snapshots shown in Fig. 2, these calculations show considerable correlation between wetting states in nearby wells. Correlation weakens with increasing separation r. The range of correlations depends on pressure, showing the anticipated increase [57] in the proximity of the intrusion pressure characterized by liquid/gas coexistence in the wells. Because of this coexistence, fluctuations in water uptake in the wells peak at intrusion pressure in accordance with maximal compressibility at the inflection point of the intrusion curves, Figs. 4–6. The above picture is reinforced by monitoring the probability distribution for the overall water uptake at different pressures. In Fig. 8 we show the distribution $P(N)$ where N denotes the number of water molecules in central surface grooves of the smaller surface. To exclude the bias toward the water-filled state at the surface edges, the sample ignores edge grooves on both sides. While high-pressure distribution curves peak at near-filled states (Wenzel regime) and low-pressure ones at small-content states (Cassie regime), the intermediate pressure (113 atm) presents a broad distribution indicative of fluctuations between the two wetting regimes. Within statistical precision of our computations, this pressure presents a probable transition point between the two regimes. Analogous analysis for the bigger surface showed

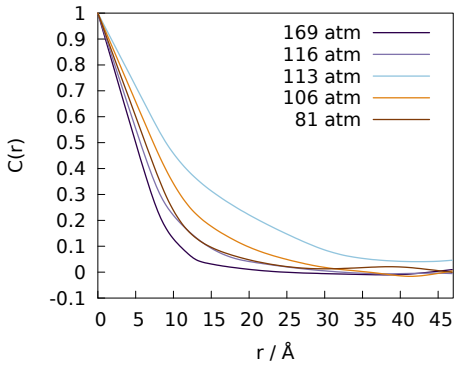

Fig. 7 Correlations among water populations N_i in distinct surface wells at r_a and r_b on the superhydrophobic substrate as a function of the distance between the wells $r = |r_a-r_b|$ at pressures from 81 to 169 atm.

broadest distribution $P(N)$ and longest range of correlation function $C(r;P)$ around 153±2 atm, matching the inflection point of the intrusion curve in Fig. 6. The intrusion pressure is ~39 atm higher than observed in the smaller system. Assuming the C2W pressure reduction to be approximately proportional to the fraction of edge grooves (40% in the smaller and 20% in the bigger system), extrapolation to macroscopic surfaces would yield an estimated C2W transition pressure around 190 atm. Prohibitive computational costs prevented direct validation by simulations in bigger systems.

Because of the involvement of metastable Wenzel states (Figs. 4-6), we have not attempted to determine correlation functions and water uptake probabilities $P(N)$ in fixed Z simulations for states on the decompression (W2C) branch. Visualized trajectories suggest the range of correlations between wetting states of neighboring sites during the W2C transition to be similar as on the compression (C2W) branch, with the transition beginning in central grooves in an approximate reversal of the pathway observed at higher pressures (smaller Z) during the C2W transition.

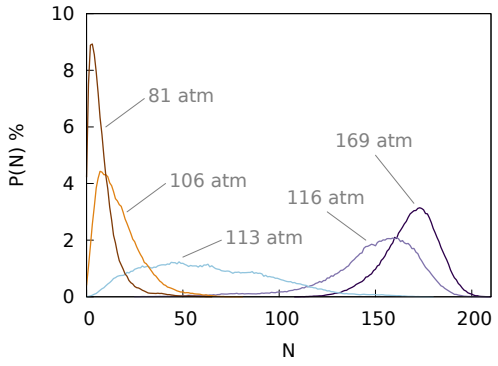

Fig. 8 Probability distribution of water uptake N inside the surface wells on the superhydrophobic surface at pressures from 81 to 169 atm. Edge grooves were excluded from the sample. C2W transition is indicated at $P \sim 114$ atm.

3.3 Transition dynamics

The response time of wetting transition is closely related to the correlation time of spontaneous fluctuations of water uptake in surface wells. We begin by defining the temporal correlation function for the total number of water molecules, $N(t;P)$, inside the wells on the corrugated surface at time t and specified pressure P

$$C(t;P) = \frac{<\delta N(t;P)\delta N(0;P)>}{<\delta N(0;P)^2>} \quad (2)$$

where δ denotes the time dependent fluctuation of $N(t;P)$, $\delta N(t;P) = N(t;P) - <N(0;P)>$ and $<N(0;P)>$ is the equilibrium average of N. To avoid a possible distortion due to thermostatting, correlation functions were calculated in 22 ns equilibrium *NVE* simulations started from equilibrated states from preceding pressure calculations in *NVT* ensemble. In view of increasing noise in $C(t;P)$ at long times t, plausible data were limited to subnanosecond times, which affects the accuracy of estimated correlation times $\tau_{corr}(P)$ defined by the relation

$$\tau_{corr}(P) = \int_0^\infty C(t;P)dt \quad (3)$$

For this reason, we also attempted to identify a suitable analytic approximation for $C(t;P)$. A reasonable fit was typically obtained using a two-parameter stretched exponential function

$$C(t;P) \sim e^{-(\frac{t}{\tau})^\beta} \quad (4)$$

with β near unity corresponding to monoexponential relaxation. While β serves as a mere fitting parameter with undetermined physical meaning, regression analysis consistently lead to β values close to 2/3, with the mean value (average over 5 different pressures Pz) in the smaller system $<\beta> = 0.694 \pm 0.024$ and the mean value (over 7 pressures) in the bigger system $<\beta> = 0.662 \pm 0.003$. The reported uncertainty corresponds to the standard deviation of the mean over all runs at specified system size (5 in the smaller and 7 in the bigger system). Standard deviations for the results of individual runs were estimated at 0.05 in the smaller and 0.01 in the bigger system. In Fig. 9, we show two examples of the plots of ln (-ln $C(t)$) vs ln t, which take a linear form if $C(t)$ behaves according to Eq. 4. The example cases correspond to pressures slightly above the Cassie-to-Wenzel transition for the two sizes of the surface. Table 1 presents estimated values of β obtained by fitting curves exemplified in Fig. 9 all twelve situations. It also lists estimated relaxation times defined by Eq. 4. Irrespective of β, the estimated values of τ correspond to the time at which the correlation function passes through the value $e^{-1} \approx 0.368$ (vanishing ln (-ln $C(t)$)). We denote these estimates as τ_o. With the exception of the C2W transition point in the bigger system, τ_o values are in reasonable agreement with the values of τ obtained from the best fit of

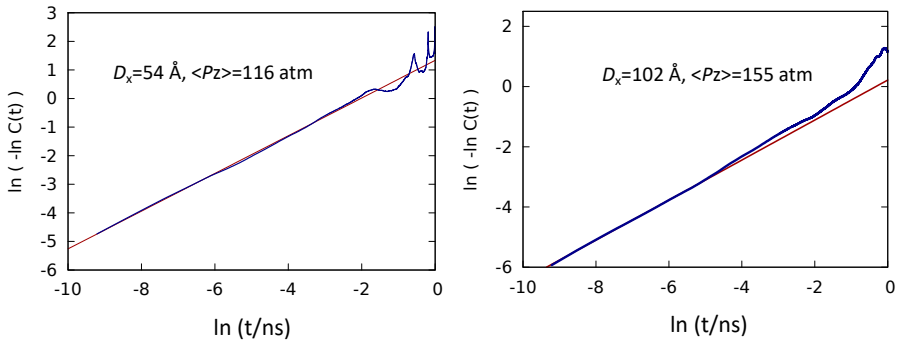

Fig. 9 Time correlation function for the fluctuating water uptake in surface wells associated with changes between the Cassie and Wenzel wetting regimes. Statistics is typically best at short times, where the linear form indicates stretched exponential relaxation $C(t) \sim \exp[-(t/\tau)^{\beta}]$ with slope corresponding to $\beta \sim 2/3$.

entire curves $C(t)$ including statistically poorer data in long-time regime. Lastly, we list the estimates of the correlation times, $\tau_{corr}(P)$, (Eq. 3) approximated by integrals over the time interval from 0 to a maximal time t_{max} within which we were able to obtain statistically reasonable estimates of $C(t;P)$ for specified values of P. The truncation error should approach zero with increasing *ratios* of t_{max} and the correlation time. These ratios are hence included in the final column of Table 1. In view of applied truncation and statistical uncertainties of $C(t;P)$, error bars of at least 20% are likely for the reported times τ_o and τ_{corr}. Because the observed decay of $C(t;P)$ deviates from monoexponential relaxation ($\beta \neq 1$), the two characteristic times should differ even with improved statistics. Nonetheless, both τ_o and τ_{corr} manifest identical qualitative behaviors showing fast relaxation at pressures well below, or above, the wetting transition value as fluctuations in water uptake by the wells are relatively small in these two regimes. Relaxation times significantly increase in the proximity to the transition pressure for the C2W process characterized by giant water-uptake fluctuations (Fig. 8). Maximal values of τ_o and τ_{corr} are within ~170±40 ps and 420±80 ps for the smaller and bigger surface, respectively. Since observed trajectories suggest cooperative transitions where the boundary between distinct states traverses a length commensurate with surface size, the above response times suggests approximately identical speeds of perimeter propagation in both system. This would be expected for steady propagation rates balancing the size-independent perimeter 'friction' (per unit length) and thermodynamic

Table 1. Characteristic times for fluctuation relaxation of water population in surface wells at specified system sizes (D_x), distances between top and bottom box boundaries (Z), and associated equilibrium pressures along z axis, $\langle P_z \rangle$. τ and τ_o are relaxation times deduced by presuming the stretched exponential relaxation, Eq. 4, with the former corresponding to the best fit of available data and the latter to the time when $C(t)$ equals e^{-1}, respectively. β is the stretched exponential parameter best fitting the simulation data at given conditions. τ_{corr} approximates the correlation time, Eq. 3, based on integration of $C(t)$ from t=0 to t_{max} beyond which reliable data of $C(t)$ are not available.

D_x / Å	Z / Å	$\langle P_z \rangle$ /atm	τ_o / ps	τ / ps	β	τ_{corr} / ps	t_{max}/τ_{corr}
54	79.4	169	21	24	0.633	21	9.5
54	80.2	116	118	132	0.660	166	6
54	81.0	113	194	275	0.750	138	29
54	81.8	106	43	49	0.747	57	8.8
54	82.6	81	43	46	0.681	51	16
102	94.8	288	10	9	0.662	14	11
102	95.4	238	15	12	0.672	14	19
102	96.0	194	36	34	0.659	33	48
102	96.6	152	80	117	0.663	79	6.3
102	97.2	153	486	1466	0.636	359	4.5
102	97.8	155	411	721	0.664	390	3.1
102	98.4	142	81	89	0.650	95	4.2

'force' due to the surface free energy difference $\gamma(\cos\theta_{Cassie}$-$\cos\theta_{Wenzel})$ between the two wetting states in analogy to triple-line dynamics in wetting [58-60]. While edge C2W nucleation is significant on nanosized surfaces considered in this work, on bigger surfaces, the process should increasingly depend on nucleation events away from the edges. In macroscopic limit, the dynamics of both the W2C and C2W transitions is expected to be controlled by homogeneous nucleation events. Because of the kinetic barrier to water expulsion from the wells, the W2C process determines the achievable cycling rate. The limiting rate of the transition on macroscopic surfaces will depend on the frequency of nucleation events per unit area, and the perimeter speed associated with the growth of Cassie state islands on the surface. As edge effects impede well-evacuation events, the response time on the finite surface determined in our study provides the lower bound of the frequency term. Assuming no significant dependence of the velocity of perimeter propagation on surface size, the response times observed on our model surfaces should therefore also provide a fair estimate for practically relevant macroscopic systems.

4 Conclusions

Transitioning between the Cassie and Wenzel wetting states on corrugated surfaces can enable large changes of surface wettability under subtle pressure control. The challenge in securing reversible tuning is to identify corrugation dimensions sufficiently small to avoid prohibitive hysteresis due to the metastability of the Wenzel state, while keeping the Cassie-to-Wenzel transition pressure within practical limits. Using Molecular Dynamics simulations we show a nanocorrugated surface with ~ sub nm asperities and spacings among them to support the Wenzel state under compression of about 100 atm while the forward-backward cycling reveals only moderate hysteresis. The hysteresis is reflected in delayed wetting-state reversal during decompression. Because of the partial connectedness of surface wells on the pillared substrate, the transitions in both directions proceed in a cooperative manner with strong correlations between wetting states of neighboring wells. The range of correlation strongly depends on the pressure. Calculations for states along the Cassie-to-Wenzel trajectories show the correlation length to increase with the proximity to the threshold pressure of the wetting transition. At the treshold pressure, detectable correlations extend over the entire width of the simulated surface. For ~10 nm surfaces, response times of wetting states to changing pressure were determined from relaxation of spontaneous fluctuations of water uptake in the grooves. Since water-evacuation events initiating the Wenzel-to-Cassie transition occur away from surface edges, the subnanosecond times identified in finite-size calculations are argued to also provide a usable estimate for the response rates at practically important meso- or macroscopic surface dimensions inaccessible by molecular simulations.

Acknowledgment

We acknowledge National Science Foundation for support (award CHE-1800120) and Extreme Science and Engineering Discovery Environment (XSEDE), funded by NSF Grant No. OCI-1053575, and the National Energy Research Scientific Computing Center (NERSC), funded by the Office of Science of the U.S. Department of Energy (No. DEAC02-05CH11231) for supercomputing time allocations.

Conflicts of interest

There are no conflicts to declare.

References

[1] C.G. Jothi Prakash, R. Prasanth, Approaches to design a surface with tunable wettability: a review on surface properties. J. Mater. Sci. **56**, 108-135 (2021).
[2] Q.H. Zeng, H. Zhou, J.X. Huang, Z.G. Guo, Review on the recent development of durable superhydrophobic materials for practical applications. Nanoscale **13**, 11734-11764 (2021).
[3] S.N. Smirnov, I.V. Vlassiouk, N.V. Lavrik, Voltage-Gated Hydrophobic Nanopores. ACS Nano **5**, 7453-7461 (2011).
[4] M.R. Powell, L. Cleary, M. Davenport, K.J. Shea, Z.S. Siwy, Electric-field-induced wetting and dewetting in single hydrophobic nanopores. Nature Nanotechnol. **6**, 798-802 (2011).
[5] Y. Grosu, M. Mierzwa, V.A. Eroshenko, S. Pawlus, M. Chorazewski, J.M. Nedelec, J.P.E. Grolier, Mechanical, Thermal, and Electrical Energy Storage in a Single Working Body: Electrification and Thermal Effects upon Pressure-Induced Water Intrusion Extrusion in Nanoporous Solids. ACS Appl. Mater. Interfaces **9**, 7044-7049 (2017).
[6] A. Tinti, A. Giacomello, Y. Grosu, C.M. Casciola, Intrusion and extrusion of water in hydrophobic nanopores. Proc. Natl. Acad. Sci. U.S.A. **114**, E10266-E10273 (2017).
[7] E. Bormashenko, Progress in understanding wetting transitions on rough surfaces. Adv. Coll. Interface Sci. **222**, 92-103 (2015).
[8] B. Liu, F.F. Lange, Pressure induced transition between superhydrophobic states: Configuration diagrams and effect of surface feature size. J. Coll. Interface Sci. **298**, 899-909 (2006).
[9] W.Q. Ren, Wetting Transition on Patterned Surfaces: Transition States and Energy Barriers. Langmuir **30**, 2879-2885 (2014).
[10] A. Checco, B.M. Ocko, A. Rahman, C.T. Black, M. Tasinkevych, A. Giacomello, S. Dietrich, Collapse and Reversibility of the Superhydrophobic State on Nanotextured Surfaces. Phys. Rev. Lett. **112**, 216101 (2014).
[11] A. Lafuma, D. Quere, Superhydrophobic states. Nature Materials **2**, 457-460 (2003).
[12] D. Quere, Wetting and roughness. Ann. Rev. Mater. Res. **38**, 71-99 (2008).
[13] F. Leroy, F. Muller-Plathe, Rationalization of the Behavior of Solid-Liquid Surface Free Energy of Water in Cassie and Wenzel Wetting States on Rugged Solid Surfaces at the Nanometer Scale. Langmuir **27**, 637-645 (2011).
[14] P. Forsberg, F. Nikolajeff, M. Karlsson, Cassie-Wenzel and Wenzel-Cassie transitions on immersed superhydrophobic surfaces under hydrostatic pressure. Soft Matter **7**, 104-109 (2011).
[15] G. Whyman, E. Bormashenko, How to Make the Cassie Wetting State Stable? Langmuir **27**, 8171-8176 (2011).
[16] M.S. Dhindsa, N.R. Smith, J. Heikenfeld, P.D. Rack, J.D. Fowlkes, M.J. Doktycz, A.V. Melechko, M.L. Simpson, Reversible electrowetting of vertically aligned superhydrophobic carbon nanofibers. Langmuir **22**, 9030-9034 (2006).
[17] J. Heikenfeld, M. Dhindsa, Electrowetting on superhydrophobic surfaces: Present status and prospects. J. Adhesion Sci. and Technol. **22**, 319-334 (2008).
[18] F. Mugele, Electrical switching of wetting states on superhydrophobic surfaces: a route towards reversible Cassie-to-Wenzel transitions. Phys. Rev. Lett. **106**, 014501 (2011).
[19] D. Vanzo, A. Luzar, D. Bratko, Reversible electrowetting transitions on superhydrophobic surfaces. Phys. Chem. Chem. Phys. **23**, 27005-27013 (2021).
[20] G. Whyman, E. Bormashenko, Wetting Transitions on Rough Substrates: General Considerations. Journal of Adhesion Science and Technology **26**, 207-220 (2012).

[21] C.D. Daub, J. Wang, S. Kudesia, D. Bratko, A. Luzar, The influence of molecular-scale roughness on the surface spreading of an aqueous nanodrop. Faraday Discussions **146**, 67-77 (2010).
[22] T. Verho, J.T. Korhonen, L. Sainiemi, V. Jokinen, C. Bower, K. Franze, S. Franssila, P. Andrew, O. Ikkala, R.H.A. Ras, Reversible switching between superhydrophobic states on a hierarchically structured surface. Proc. Natl. Acad. Sci. U.S.A. **109**, 10210-10213 (2012).
[23] K. Leung, A. Luzar, Dynamics of capillary evaporation. II. Free energy barriers. J. Chem. Phys. **113**, 5845-5852 (2000).
[24] S. Sharma, P.G. Debenedetti, Free Energy Barriers to Evaporation of Water in Hydrophobic Confinement. J. Phys. Chem. B **116**, 13282-13289 (2012).
[25] T. Werder, J.H. Walther, R.L. Jaffe, T. Halicioglu, P. Koumoutsakos, On the water-carbon interaction for use in molecular dynamics simulations of graphite and carbon nanotubes. J. Phys. Chem. B **107**, 1345-1352 (2003).
[26] V.B. Mbayachi, E. Ndayiragije, T. Sammani, S. Taj, E.R. Mbuta, A. Khan, Graphene synthesis, characterization and its applications: A review. Results Chem. **3**, 100163 (2021).
[27] A.R. Leach, Molecular Modelling: Principles and Applications, Prentice Hall, London, 2001.
[28] B. Lee, F.M. Richards, Interpretation of Protein Structures - Estimation of Static Accessibility. Journal of Molecular Biology **55**, 379-& (1971).
[29] M.L. Connolly, Solvent-Accessible Surfaces of Protein and Nucleic-Acids. Science **221**, 709-713 (1983).
[30] J.H. Wang, D. Bratko, A. Luzar, Probing surface tension additivity on chemically heterogeneous surfaces by a molecular approach. Proc. Natl. Acad. Sci. U.S.A. **108**, 6374-6379 (2011).
[31] Y.S. Li, D. Quere, C.J. Lv, Q.S. Zheng, Monostable superrepellent materials. Proc. Natl. Acad. Sci. U.S.A. **114**, 3387-3392 (2017).
[32] S. Plimpton, Fast Parallel Algorithms for Short-Range Molecular-Dynamics. J. Comput. Phys. **117**, 1-19 (1995).
[33] I.C. Yeh, M.L. Berkowitz, Ewald summation for systems with slab geometry. J. Chem. Phys. **111**, 3155-3162 (1999).
[34] M.P. Allen, D.J. Tildesley, Computer simulation of liquids, Oxford University Press, New York, 2017.
[35] K. Lum, D. Chandler, Phase diagram and free energies of vapor films and tubes for a confined fluid. Int. J.Thermophys. **19**, 845-855 (1998).
[36] D. Bratko, R.A. Curtis, H.W. Blanch, J.M. Prausnitz, Interaction between hydrophobic surfaces with metastable intervening liquid. J. Chem. Phys. **115**, 3873-3877 (2001).
[37] H. Acharya, S. Ranganathan, S.N. Jamadagni, S. Garde, Mapping Hydrophobicity at the Nanoscale: Applications to Heterogeneous Surfaces and Proteins. Faraday Discussions **146**, 353 (2010).
[38] N. Giovambattista, P.J. Rossky, P.G. Debenedetti, Effect of pressure on the phase behavior and structure of water confined between nanoscale hydrophobic and hydrophilic plates. Phys. Rev. E **73**, 041604 (2006).
[39] R. Evans, M.C. Stewart, The local compressibility of liquids near non-adsorbing substrates: a useful measure of solvophobicity and hydrophobicity? J. Phys. Cond. Matt. **27**, 194111 (2015).
[40] D. Vanzo, D. Bratko, A. Luzar, Wettability of pristine and alkyl-functionalized graphane. J. Chem. Phys. **137**, 034707 (2012).

[41] D. Vanzo, D. Bratko, A. Luzar, Nanoconfined water under electric field at constant chemical potential undergoes electrostriction. J. Chem. Phys. **140**, 074710 (2014).
[42] D. Vanzo, D. Bratko, A. Luzar, Dynamic Control of Nanopore Wetting in Water and Saline Solutions under an Electric Field. J. Phys. Chem. B **119**, 8890-8899 (2015).
[43] N. Ojaghlou, D. Bratko, M. Salanne, M. Shafiei, A. Luzar, Solvent-Solvent Correlations across Graphene: The Effect of Image Charges. ACS Nano **14**, 7987-7998 (2020).
[44] S. Zamfir, F. Moucka, D. Bratko, High-Pressure Infiltration-Expulsion of Aqueous NaCl in Planar Hydrophobic Nanopores. J. Phys. Chem. C **124**, 23433-23445 (2020).
[45] H.J.C. Berendsen, J.R. Grigera, T.P. Straatsma, The Missing Term In Effective Pair Potentials. J. Phys. Chem. **91**, 6269-6271 (1987).
[46] C.D. Daub, D. Bratko, K. Leung, A. Luzar, Electrowetting at the nanoscale. J. Phys. Chem. C **111**, 505-509 (2007).
[47] J.A. Ritchie, J.S. Yazdi, D. Bratko, A. Luzar, Metastable Sessile Nanodroplets on Nanopatterned Surfaces. J. Phys. Chem. C **116**, 8634-8641 (2012).
[48] J. Driskill, D. Vanzo, D. Bratko, A. Luzar, Wetting transparency of graphene in water. J. Chem. Phys. **141**, 18C517 (2014).
[49] B.S. Jabes, J. Driskill, D. Vanzo, D. Bratko, A. Luzar, Metastable Vapor in a Janus Nanoconfinement. J. Phys. Chem. C **121**, 13144-13150 (2017).
[50] Y. Kopel, N. Giovambattista, Comparative Study of Water-Mediated Interactions between Hydrophilic and Hydrophobic Nanoscale Surfaces. J. Phys. Chem. B **123**, 10814-10824 (2019).
[51] D. Bratko, C.D. Daub, K. Leung, A. Luzar, Effect of field direction on electrowetting in a nanopore. J. Am. Chem. Soc. **129**, 2504-2510 (2007).
[52] R. Evans, Fluids Adsorbed in Narrow Pores - Phase-Equilibria and Structure. J. Phys. Cond. Matt. **2**, 8989-9007 (1990).
[53] K. Lum, A. Luzar, Pathway to surface-induced phase transition of a confined fluid. Phys. Rev. E **56**, R6283-R6286 (1997).
[54] K. Leung, A. Luzar, D. Bratko, Dynamics of capillary drying in water. Phys. Rev. Lett. **90**, 065502 (2003).
[55] E. Bormashenko, R. Pogreb, G. Whyman, M. Erlich, Resonance Cassie-Wenzel wetting transition for horizontally vibrated drops deposited on a rough surface. Langmuir **23**, 12217-12221 (2007).
[56] C. Ishino, K. Okumura, Nucleation scenarios for wetting transition on textured surfaces: The effect of contact angle hysteresis. Europhys. Lett. **76**, 464-470 (2006).
[57] S. Gupta, A. Irback, B. Petersson, R.V. Gavai, F. Karsch, The Correlation Lengths and the order of the Phase Transition in 3-Dimensional Z-3 Symmetric Models. Nuclear Phys. B **329**, 263-284 (1990).
[58] R.G. Cox, The Dynamics of the Spreading of Liquids on a Solid Surface. Part 2. Surfactants. J. Fluid Mech. **168**, 192-220 (1986).
[59] P.G. de Gennes, F. Brochard-Wyart, Dynamics of Partial Wetting. Adv. Colloid Interface Sci. **39**, 1-11 (1992).
[60] M. Ramiasa, J. Ralston, R. Fetzer, R. Sedev, The influence of topography on dynamic wetting. Adv. Coll. Interface Sci. **206**, 275-293 (2014).